Batteries & Supercaps

Research Article
doi.org/10.1002/batt.202500497

Chemistry Europe
European Chemical Societies Publishing

www.batteries-supercaps.org

Influence of Salt Concentration on the Electrochemical Performance of Magnesium Hexafluoroisopropoxy Aluminate Electrolyte

Andrijana Marojević, Tjaša Pavčnik, Olivera Lužanin, Jože Grdadolnik, Klemen Pirnat, Alexandre Ponrouch, Robert Dominko, and Jan Bitenc*

One of the challenges in the development of Mg batteries is the lack of Mg electrolytes with good compatibility with both the Mg metal anode and cathode materials. In recent years, Mg salts based on weakly coordinating anions have emerged as promising Mg electrolytes. In this work, we systematically investigate the effects of salt concentration on the physicochemical properties, salt–solvent interactions, and electrochemical performance of the $Mg[Al(hfip)_4]_2$/G2 electrolyte. Infrared (IR) and Raman spectroscopy are used to study the changes in the electrolyte speciation across different concentrations, indicating a decreased amount of free glyme solvent with higher salt concentration. Mg plating/stripping of selected electrolytes is evaluated through three different testing protocols (conventional cycling, macrocycling, and cycling with added open-circuit voltage (OCV) rests) and compatibility with different cathode materials such as Chevrel phase, sulfur, and various organic redox-active compounds. In the electrochemical tests, more concentrated electrolytes demonstrated improved cathode cycling efficiency and more stable Mg plating/stripping, making an argument for Mg electrolytes with higher salt concentration. However, higher salt concentrations can increase the cost of Mg electrolytes. Further Mg electrolyte optimization should focus on adjusting electrolyte composition to specific electrode materials and other cell components, while maintaining a reasonable cost.

1. Introduction

Magnesium (Mg) battery research has gained traction as a potential alternative to Li-ion batteries due to the low redox potential of the Mg metal anode (−2.36 V vs SHE) and the abundance of elemental Mg in the Earth's crust. Its bivalent nature is key to the attractiveness of Mg metal anode, resulting in very high gravimetric (2205 mAh g^{-1}) and volumetric capacities (3833 mAh cm^{-3}).[1] It is also less prone to dendrite formation during metal plating/stripping and has improved safety properties over highly reactive alkali metals.[2] However, its low redox potential poses a challenge as the decomposition of electrolyte species or atmospheric impurities can quite often lead to the formation of blocking passive layers on the Mg metal. Due to the bivalent nature of Mg, the electrolyte speciation is more complex and influences the formation of passive layers, emphasizing the need for in-depth investigation of electrolyte formulations. Therefore, the realization of practical Mg batteries remains distant due to the complex interfacial chemistry between the Mg metal anode and the electrolyte, combined with a lack of high-energy density cathode hosts.

Recently, significant improvement has been achieved in the field of electrolytes with the development of Mg salts based on weakly coordinating anions (WCA), which enable reversible Mg plating/stripping without utilizing highly reactive reagents like organometallic or corrosive chloride-based salts,[3,4] opening an avenue toward practical Mg batteries. Different WCA-based Mg salts were synthesized, like Mg monocarboranes,[5] fluorinated alkoxyborates,[6–10] and alkoxyaluminates,[11–14] exhibiting high Mg plating/stripping efficiencies far above 95%. Some WCA-based electrolytes achieved metal plating/stripping efficiencies beyond 99% (such as 0.25 M $Mg[Al(hfip)_4]_2$/G1 exhibiting up to 99.3% and 0.3 M $Mg[Al(hfip)_4]_2$/G2 exhibiting up to 99.4% efficiency),[11,12] which were in the past characteristic only for Mg electrolytes utilizing much more reactive organometallic compounds. While monocarborane-based Mg electrolytes remained less explored due to relatively expensive reagents, fluorinated alkoxyborates and aluminates gained more attention. Different

A. Marojević, T. Pavčnik, O. Lužanin, J. Grdadolnik, K. Pirnat, R. Dominko, J. Bitenc
National Institute of Chemistry
Hajdrihova 19, 1001 Ljubljana, Slovenia
E-mail: jan.bitenc@ki.si

A. Marojević, R. Dominko
Faculty of Chemistry and Chemical Technology
University of Ljubljana
Večna pot 113, 1001 Ljubljana, Slovenia

T. Pavčnik, A. Ponrouch
Institut de Ciència de Materials de Barcelona, ICMAB-CSIC
Campus UAB, 08193 Bellaterra, Spain

A. Ponrouch, R. Dominko
Alistore-European Research Institute
CNRS FR 3104
Hub de l'Energie
Rue Baudelocque, 80039 Amiens, France

Supporting information for this article is available on the WWW under https://doi.org/10.1002/batt.202500497

research groups investigated the effects of different fluorinated alkoxy ligands[7,8,10] and the central atom variation between B and Al on the performance of Mg salts.[12,13] It was found that a low degree of anion fluorination leads to limited salt dissociation, resulting in low electrolyte conductivity, as demonstrated in the case of Mg tetrakis(trifluoroethanoxy)borate ($Mg[B(tfe)_4]_2$). On the contrary, increased anion fluorination improves dissociation, but can result in much bulkier anions with lower mobility, again leading to decreased electrolyte conductivity.[8]

Currently, the highest conductivity among borate salts was demonstrated with the Mg tetrakis(hexafluoroisopropoxy)borate ($Mg[B(hfip)_4]_2$) salt. Replacement of the B central atom in the anion with Al has demonstrated an additional increase in the electrolyte conductivity (from 5.41 mS cm^{-1} for 0.4 M $Mg[B(hfip)_4]_2$/G2 to 6.12 mS cm^{-1} for 0.4 M $Mg[Al(hfip)_4]_2$/G2 at room temperature), and a positive impact on both Mg plating/stripping efficiency and overpotential.[11–13,15] At the same time, it is important to consider the influence of salt synthesis on the performance of the Mg electrolytes. Synthesis route investigations demonstrated a positive effect of the organometallic salt synthesis route over the metathesis reaction from alkali metal precursors and synthesis from borohydride starting reagents. It was shown that low purity of Mg borohydride precursor and the presence of alkali salt impurities can lead to decreased electrochemical performance of Mg electrolytes.[14,16,17]

Although prior studies have investigated different WCA-based Mg salts and synthesis routes, the effect of salt concentration remains underexplored. Salt concentration can affect the formation of electrolyte species, with higher concentrations of salts leading to the formation of ion-pairs and decreased coordination of Mg^{2+} species with glyme solvents. In our work, we selected magnesium tetrakis(hexafluoroisopropoxy)aluminate ($Mg[Al(hfip)_4]_2$, later denoted as MgAlhfip) as one of the best-performing WCA-based salts. The MgAlhfip concentration effect is investigated from multiple points of view: physicochemical properties and spectroscopy investigation, as well as metal plating/stripping, and cathode active materials electrochemical testing. Different Mg plating/stripping protocols are employed to evaluate the electrolyte concentration effect on the Mg metal anode, followed by tests with various cathode active materials undergoing electrochemical mechanisms such as insertion, coordination, and conversion.

2. Results and Discussion

2.1. Salt and Electrolyte Characterization

To investigate the influence of different salt concentrations on the electrochemical performance, MgAlhfip synthesized through an organometallic route with a salt isolation step was selected, as it yields a salt with optimal electrochemical performance, as reported previously.[14] The MgAlhfip salt was characterized using Nuclear magnetic resonance (NMR) spectroscopy (Figure S1, Supporting Information). The results of ^{1}H NMR spectra are in agreement with previous reports.[11,12] Peaks at 3.2 and 3.4 ppm in the ^{1}H spectra were assigned to the G1 molecules, and based on the integrals of these peaks, it was confirmed that the Mg^{2+} cation is coordinated with three molecules of G1 solvent, forming the $[Mg(G1)_3][Al(hfip)_4]_2$ structure. The peak at 3.3 ppm can be attributed to water present in the synthesized salt (Table S1, Supporting Information) and DMSO-d_6 solvent, while the peak at 4.6 ppm is attributed to the proton of the hfip ligand within the $[Al(hfip)_4]^-$ anion. Minor peaks in the ^{1}H at 0.8 ppm were the result of traces of the hexane solvent remaining from the salt isolation process, and trace peaks around 5 and 8 ppm can be attributed to the unreacted hfip that could not be fully removed through the final drying of the salt.

Different molar concentrations of electrolytes were prepared using synthesized salt and diglyme (G2) as solvent, as G2-based electrolytes previously demonstrated Mg plating/stripping with the highest efficiency and lowest overpotential among different glyme-based solvents (monoglyme-G1, G2, and triglyme-G3).[12,13] Physicochemical characterization was performed over a temperature range of 5–60 °C and in the concentration range of 0.1–0.6 M (**Figure 1**). As shown in Figure 1a, the ionic conductivity increased with temperature, which can be attributed to the improved salt dissociation and ion mobility. In the low concentration range below 0.3 M, particularly at higher temperatures, the ionic conductivity increased almost linearly with salt concentration, indicating good salt dissociation and ion mobility of the MgAlhfip electrolyte. However, at higher salt concentrations, a plateau in ionic conductivity is reached, followed by a decrease, as observed for 0.6 M concentration. This behavior can be explained by two key factors known to influence ionic conductivity: salt dissociation and charge carrier mobility. Above a certain concentration (0.4 M), the conductivity decreases due to stronger cation–anion interactions (ion pair formation) and leads to a lower number of active charge carriers. At the same time, as the salt concentration increases, the viscosity of the electrolyte also increases (Figure 1b), which hinders the movement of ions and contributes to the decrease in ionic conductivity. At higher temperatures, a decrease in the viscosity of the electrolyte was observed, which, together with more facile salt dissociation, resulted in increased conductivity. This trend is more pronounced at higher concentrations, particularly at 0.6 M.

To investigate the electrochemical performance of the MgAlhfip/G2 electrolyte, three different concentrations (0.2, 0.4, and 0.6 M, Table S2, Supporting Information) were selected based on their similar ionic conductivities measured at 25 °C (4.1, 6.1, and 5.5 mS cm^{-1}, respectively). Despite comparable conductivities, the electrolytes exhibit significantly different viscosities (1.7, 2.6, and 4.2 mPa s at 25 °C, respectively). The combination of similar ionic conductivities at different salt concentrations suggests differences in ion interactions within the electrolyte solutions. Different ion interactions, along with viscosity variations, can significantly influence the electrochemical reactions in a Mg battery cell. In order to better understand the influence of the different electrolyte concentrations, IR and Raman spectroscopy were employed for further investigation.

The IR spectra of 0.2, 0.4, and 0.6 M MgAlhfip electrolytes, along with pristine MgAlhfip salt, G1, and G2, are shown in Figure S2, Supporting Information. A broad peak at 1177 cm^{-1}

Research Article
doi.org/10.1002/batt.202500497
Chemistry Europe
European Chemical Societies Publishing

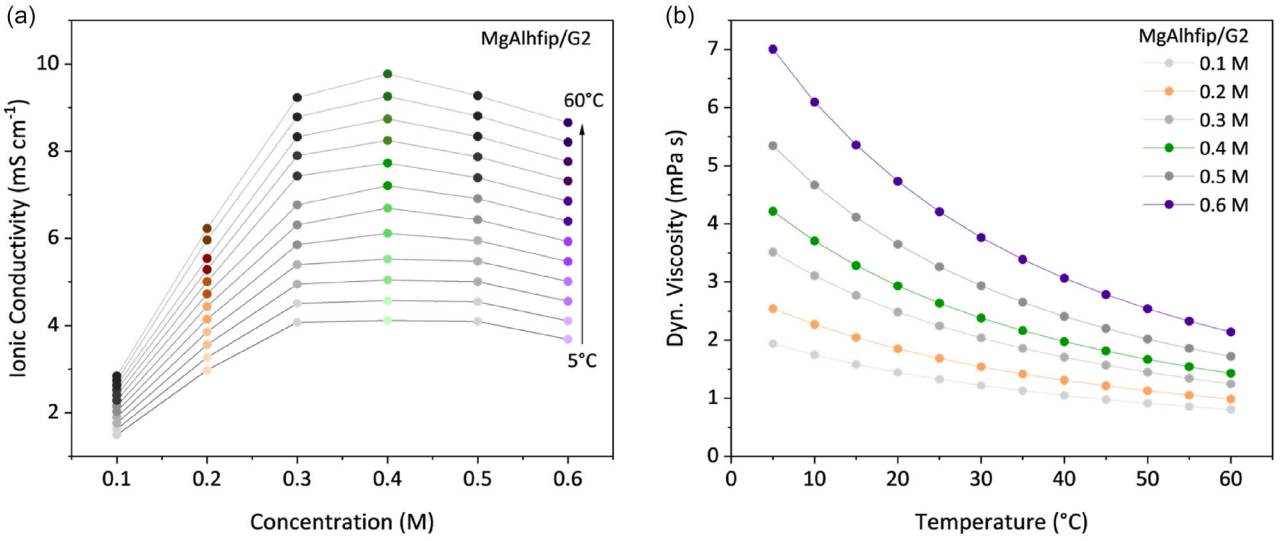

Figure 1. Physicochemical characterization of MgAlhfip/G2 electrolyte with different concentrations in the temperature range from 5 to 60 °C. a) Ionic conductivity and b) dynamic viscosity.

in the spectrum of the pristine salt is attributed to the Al—O—C vibration, along with the symmetric and asymmetric $-CF_3$ stretching modes. Further peaks are observed at 1375 cm^{-1} (C–CF_3 vibrations) and 684 cm^{-1} (–CF_3 deformation). A broad intensity band at 1470 cm^{-1} is associated with the C—H deformation of methyl and methylene groups in glyme molecules, which are coordinated to the Mg^{2+} cations, according to the literature.[13,14] In the 1200–1000 cm^{-1} range, the IR bands are assigned to the vibrational modes of the ether molecules (such as C—O—C, C—C—C, and C—O stretching vibrations)[18] and the Al—O—C bond of the anion,[13,14] together with the intense C—C/C—O and the C—C/C—F modes that occur at about 1000 cm^{-1}[19] (Figure S2, Supporting Information). The characteristic band for glyme (at 1106 cm^{-1} for G1 and 1102 cm^{-1} for G2) undergoes significant changes in MgAlhfip electrolytes, with new peaks appearing at lower wavenumbers (1095, 1070, and 1039 cm^{-1}, highlighted in Figure S2a, Supporting Information) with increasing salt concentration. Although some of these peaks can be attributed to the coordination of glyme molecules to Mg^{2+} cations, it is also important to consider the possible contribution of the anion. With increasing salt concentration, the peak around 1089 cm^{-1} shifts to a higher wavenumber (1095 and 1096 cm^{-1}), indicating possible Mg^{2+} coordination with the Alhfip anion.[20] In addition, isosbestic points (where the spectra of different compounds overlap) can be seen at 1140 and 1028 cm^{-1} (Figure S2b, Supporting Information), suggesting the presence of two distinct species in solution—likely free and Mg-bound forms of G2.[18]

In Raman spectroscopy, different spectral regions provide insights into specific solvent conformers and ion interactions (Figure S3, Supporting Information). According to the literature,[21] the most relevant range for analyzing solvent conformers is 780–900 cm^{-1}, while the 740–780 cm^{-1} region can be associated with anion interactions.[17,22] In the 780–920 cm^{-1} range (**Figure 2**a), bands corresponding to glyme conformers

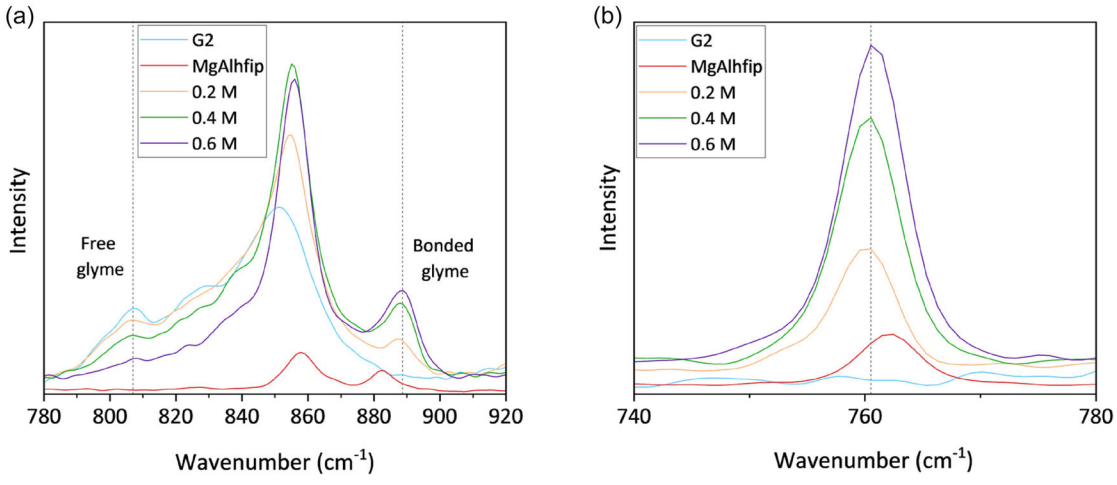

Figure 2. Raman spectra for pristine G2, MgAlhfip salt and different concentrations of MgAlhfip/G2 in a) 780–920 cm^{-1} region and b) 740–780 cm^{-1} region.

are observed. These vibrational bands, which are assigned to the C—O stretching and $-CH_3$ vibrational modes, can be very sensitive to molecular conformations and solvent-ion interactions. The Raman band appearing at 883 cm^{-1} can be assigned to the coordination of the Mg cation by the glyme solvents, as a result of the chelation of Mg^{2+} by multiple oxygen atoms in each glyme molecule.[21,23] As the concentration of the MgAlhfip salt increases, the intensity of the band corresponding to the free glyme (807 cm^{-1}) decreases, while the intensity of the Mg^{2+} bonded glyme band increases. At the same time, this band is shifted toward a higher wavenumber (887 and 889 cm^{-1}, respectively) at higher concentrations. Previous studies performed with LiAlhfip salt without coordinated solvents[19,24] and different ionic liquids based on Alhfip[19] reported bands around 855 and 766 cm^{-1} associated with the Alhfip anion. In addition, a computational analysis has suggested that a band around 874 cm^{-1} corresponds to the vibrational modes of C—C and Al—O bonds, possibly originating from the anion.[19] These results suggest that the region between 780 and 920 cm^{-1} is quite complex and sensitive, with bond vibrations prone to shifts, and that it may contain overlapping contributions from both glyme coordination and anion-related vibrations.

Figure 2b shows the spectral region around 760 cm^{-1} for the investigated electrolytes, together with the peaks that occur at this wavenumber for the pristine salt and G2 solvent. According to the literature,[17] a peak around 750 cm^{-1} for the MgBhfip salt has been associated with hfip-derived anions. Additionally, a sharp vibrational feature around 720 cm^{-1} has been attributed to the C—F mode of the Bhfip anion through DFT modeling.[22] In the spectra of MgAlhfip salt, the anion peak has been observed around 762 cm^{-1}, and in the case of electrolytes at slightly lower wavenumber. With increasing salt concentration, the electrolyte peak experiences a small blueshift, which points to subtle changes within the anion environment, most likely connected with the formation of solvent-separated ion pairs (SSIP) at increased salt concentration.[25]

2.2. Mg Metal Plating/Stripping Evaluation

The electrochemical performance of MgAlhfip electrolytes was evaluated through Mg metal plating/stripping, followed by testing of different cathode materials undergoing various electrochemical mechanisms such as ion insertion, coordination, and conversion. All tests were done in two-electrode Mg metal half-cells without an additional reference electrode.

Initially, the oxidative and reductive stability of the electrolytes were investigated through linear sweep voltammetry (LSV) (Figure S4, Supporting Information) on Pt and carbon-coated Al working electrodes. All three electrolytes exhibited high oxidative stability above 3 V (Figure S4a,c, Supporting Information), with low-intensity reductive decomposition observed below 1.0 V during the cathodic sweep (Figure S4b,d, Supporting Information). The Mg plating/stripping performance of MgAlhfip/G2 with different concentrations was evaluated through plating and stripping 1 mAh cm^{-2} of Mg metal at a moderate current density of 1 mA cm^{-2}. As expected, MgAlhfip-based electrolytes exhibited high Mg plating/stripping efficiency with relatively low overpotentials (**Figure 3**a,b). Nevertheless, clear differences were observed among different salt concentrations. All three electrolytes went through an activation period, characterized by relatively high cell overpotentials that decreased upon cycling. The most concentrated MgAlhfip electrolyte displayed the highest overpotential and lowest plating/stripping efficiency in the first cycle. In the following cycles, the overpotentials in all electrolytes decreased, leading to more similar values, with the 0.4 M electrolyte displaying the lowest stripping overpotential (74, 63, and 90 mV for 0.2, 0.4, and 0.6 M MgAlhfip, respectively), while also demonstrating the highest ionic conductivity.

To further investigate these differences, the ionic resistance contribution to cell overpotential was estimated. Considering the applied current density, ionic conductivity, and the distance between the electrodes, the estimated electrolyte resistance contribution to cell overpotential is relatively low, with values of ≈26%, 20%, and 16% for 0.2, 0.4, and 0.6 M, respectively (Table S3, Supporting Information). Interestingly, as shown in the inset in Figure 3a, the galvanostatic curve for the 0.2 M concentration displayed potential instabilities toward the end of the Mg stripping from the Pt WE, which can be associated with poor Mg deposit contact with the Pt WE or soft short-circuits toward the end of the Mg stripping process from the Pt WE. During Mg plating/stripping, 0.4 and 0.6 M MgAlhfip/G2 displayed similar Coulombic efficiencies, close to 99%, with 0.6 M electrolyte showing more stable behavior despite exhibiting slightly larger cell overpotentials among the three electrolytes. On the contrary, 0.2 M electrolyte exhibited significantly lower efficiency, with an average value of around 98% (Figure 3b).

To further investigate the Mg plating/stripping performance and mimic practical conditions in cells, we decided to employ a macrocycling procedure.[26,27] In this procedure, a five times larger amount of Mg metal (5 mAh cm^{-2}) is initially plated on the working electrode, but only one-fifth of the deposited metal is cycled in the intermediate cycles (1 mAh cm^{-2}). Cycling only 20% of the plated Mg metal in subsequent cycles ensures that plating and stripping processes resemble cycling experiments in Mg||Mg symmetrical or practical Mg cells, where Mg is plated/stripped on Mg metal anode. In this experiment, the long-term presence of Mg metal deposits on the working electrode can potentially increase the effect of the Mg metal passivation caused by side reactions between the Mg metal deposits and electrolyte, and prevent large potential variations that occur during the last part of the Mg stripping process in each cycle.[27] One drawback of this approach is that it provides only the average Coulombic efficiency.

During macrocycling, cells exhibited similar overpotentials to the ones observed in the conventional cycling procedure (Figure 3c). Interestingly, the overpotential for 0.2 M electrolyte increased toward the end of each stripping cycle in the second half of the macrocycling procedure. This trend was further confirmed in the last Mg metal stripping cycle, where the 0.2 M electrolyte exhibited a clear potential step after stripping ≈1 mAh cm^{-2} of Mg metal (Figure S5, Supporting Information).

Research Article
doi.org/10.1002/batt.202500497
Chemistry Europe
European Chemical Societies Publishing

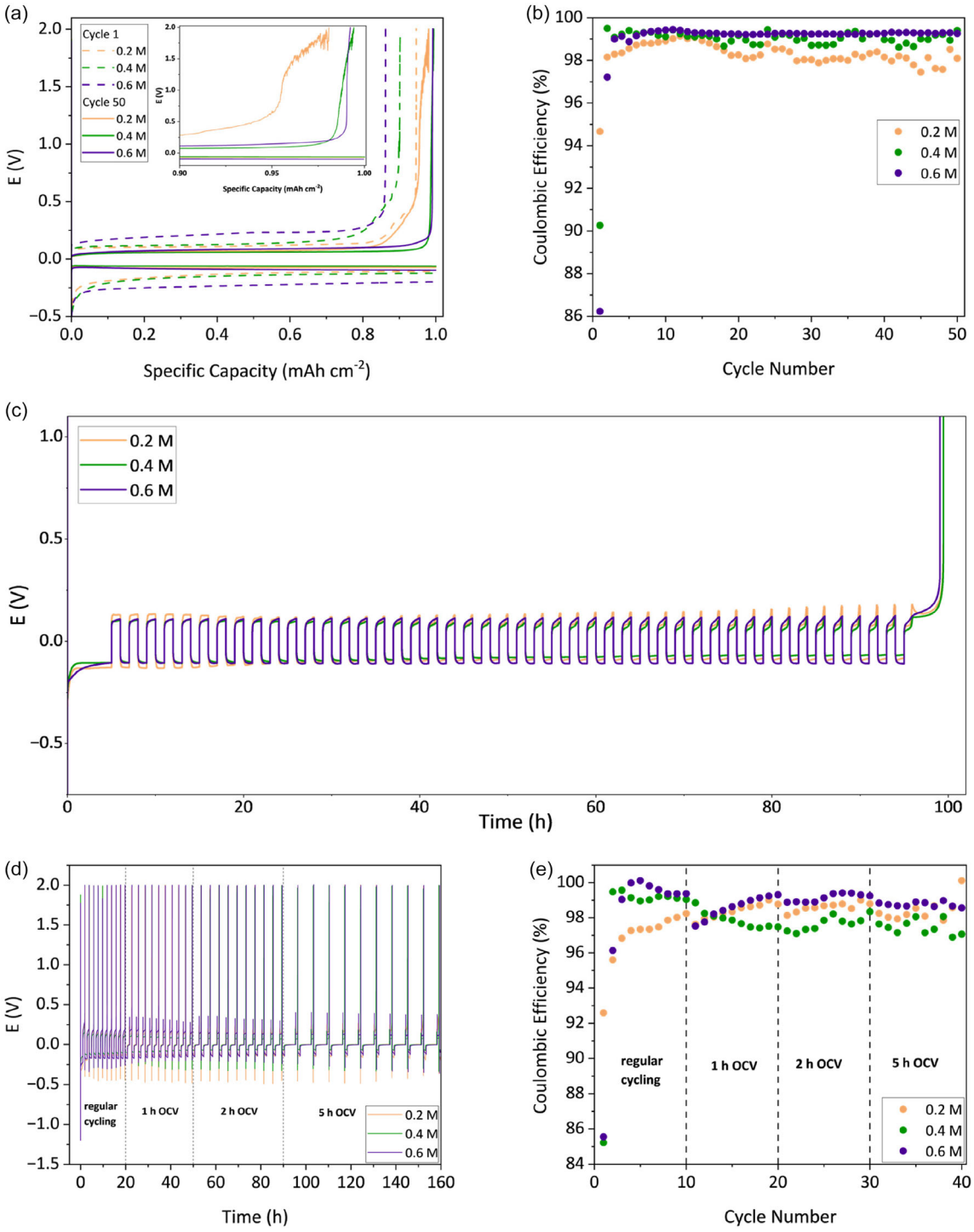

Figure 3. a) Galvanostatic curves (voltage profiles) for the 1st and 50th cycle of Mg metal plating/stripping with an inset showing the end of stripping curves in the 50th cycle and b) Coulombic efficiency of Mg plating/stripping for different MgAlhfip/G2 concentrations. c) Galvanostatic curves obtained during macrocycling in different concentrations of MgAlhfip/G2 electrolyte. Current density 1 mA cm^{-2}, initial 5 h Mg plating followed by conventional cycling (1 h stripping and subsequent 1 h plating) and final stripping of remaining Mg metal until overpotential of 2 V. d) Galvanostatic curves obtained upon cycling of different MgAlhfip/G2 electrolyte concentrations with different OCV rest periods. Current density 1 mA cm^{-2}. e) Coulombic efficiency of Mg plating/stripping. Dashed lines mark the areas of different OCV periods.

A similar, but less pronounced potential step is observed for the 0.4 M electrolyte. This behavior suggests that metal passivation can occur on the Mg metal surface during prolonged exposure of the plated Mg to the electrolyte. This observation goes in line with previous computational studies that indicated the decomposition of ether-based solvent at the Mg metal surface when solvating Mg^{2+} cations.[28] The Mg plating/stripping efficiency during the macrocycling procedure is similar to the average

values obtained during conventional cycling (**Table 1**), with a specific exception: the 0.6 M electrolyte showed reduced efficiency. This decline may be attributed to a higher level of impurities introduced by the increased salt concentration, which could be especially detrimental during the initial Mg plating process, where we deposit the largest amount of Mg (5 mAh cm^{-2}).

Although both conventional cycling and macrocycling of Mg plating/stripping are typically performed under constant current conditions, it is important to consider the behavior of Mg metal with open-circuit voltage (OCV) rests—which better reflect real battery operation, where cells are not always under current load. To investigate this, Mg plating/stripping experiments with added OCV rests after Mg plating on the Pt working electrode were conducted. This type of experiment should amplify spontaneous passivation processes due to the extended time during which Mg deposits remain in contact with the electrolyte, without an ongoing electrochemical reaction. Initially, 10 conventional cycles of Mg plating/stripping without OCV pause periods were performed. Subsequently, OCV periods of 1, 2, and 5 h were introduced after each plating half-cycle (Figure 3d).

Comparison of Mg plating/stripping Coulombic efficiencies displayed a clear drop after adding OCV periods for all electrolytes (Figure 3e). Lower electrolyte concentrations led to more erratic Coulombic efficiencies, and, in the case of 0.2 M, even led to soft short-circuits after 5 h OCV (Figure S6, Supporting Information), which are most likely caused by the partial passivation of Mg metal anode leading to more localized metal plating. Among used concentrations, 0.6 M MgAlhfip exhibited the lowest drop in Coulombic efficiency and the most stable electrochemical behavior (Figure 3e), as was already observed in the conventional cycling procedure.

Scanning electron microscopy (SEM) was employed to investigate the morphology of electrochemically deposited Mg metal on carbon-coated aluminum foil to improve adhesion (Figure S7, Supporting Information). The Mg metal deposition process was carried out for 3 min at a current density of 1 mA cm^{-2}. Mg deposits exhibit non-dendritic, round-shaped porous grains with relatively uniform size. Higher magnification micrographs indicate that each grain possesses well-defined, rounded edges with defects observed in the middle, which could indicate pitting corrosion favored at lower concentrations of electrolyte. In contrast, in the case of the 0.6 M electrolyte, the deposits were formed with fewer defects and a more uniform round shape.

Table 1. Average Coulombic efficiency of different MgAlhfip/G2 electrolyte concentrations during conventional and macrocycling Mg plating/stripping procedure. The average value for conventional cycling was reported for 50 cycles.

Concentration of MgAlhfip/G2	Conventional cycling efficiency [%]	Macrocycling efficiency [%]
0.2 M	98.3	98.9
0.4 M	98.9	98.9
0.6 M	98.9	98.1

2.3. Electrochemical Testing of Cathode Materials

In the second part of the electrochemical tests, we investigated the effect of MgAlhfip electrolyte concentration on the performance of different cathode materials, including the Chevrel phase, sulfur, and various organic redox-active compounds. These materials undergo diverse electrochemical reactions with Mg^{2+} species. The Chevrel phase, as a benchmark inorganic material, enables Mg cation insertion into the structure. Organic materials can, due to their adaptable structure, circumvent slow solid-state diffusion reactions and undergo coordination reactions. In the case of sulfur, a conversion reaction occurs, leading to the formation of various polysulfide species during its reduction. Additionally, a cycling experiment with electrodes composed solely of carbon black and a PTFE binder was conducted to evaluate the capacity contribution of carbon black. The cycling of Printex electrodes demonstrated highly reversible capacity (estimated capacity contribution of about 10–15 mAh g^{-1}), except during the initial discharge, where an additional irreversible discharge capacity of 15 mAh g^{-1} was observed from 1.0 to 0.5 V (Figure S8, Supporting Information), as already indicated in the LSV test.

Although reversible Mg^{2+} insertion into the Mo_6S_8 structure was demonstrated over two decades ago with Grignard-based electrolytes,[29] it remains an inorganic reference material for the evaluation of Mg^{2+} insertion with new electrolytes. The cycling behavior of Chevrel phase cathodes exhibited similar capacity utilization with different MgAlhfip concentrations. However, variations in cell overpotentials between charge and discharge were observed. Notably, the 0.6 M electrolyte exhibited the highest overpotentials along with the lowest active material utilization (**Figure 4**a). This behavior could be associated with the increased metal anode overpotential and electrolyte viscosity, as well as more difficult dissociation of Mg^{2+} species in the 0.6 M electrolyte, potentially limiting Mg^{2+} insertion into the Chevrel phase. Furthermore, all cells with Mo_6S_8 exhibited irreversible discharge capacity in the initial cycle (Figure S9, Supporting Information), which is consistent with the results of the reductive stability evaluation through LSV. In the following cycles, the discharge capacity stabilized (at about 50 mAh g^{-1}) and cell overpotentials decreased. The highest capacity (≈53 mAh g^{-1}) was obtained for 0.4 M electrolyte, which at the same time exhibited the lowest overpotentials (Figure 4a). Due to irreversible discharge capacity, initial Coulombic efficiency was well over 100%, but it later dropped, and stabilized around 100%, 98%, and 97% for 0.6, 0.4, and 0.2 M concentrations, respectively (Figure 4b), indicating a positive effect of the increased salt concentration on the efficiency.

Unlike the low capacity Chevrel phase, the sulfur cathode offers much higher theoretical capacity (1672 mAh g^{-1}), but its practical application faces challenges such as poor electronic conductivity of sulfur and the polysulfide shuttle effect, which are additionally intensified in Mg-S batteries by sluggish MgS reaction kinetics and low solubility of magnesium polysulfide species.[30,31] Mg-S cells with MgAlhfip electrolytes exhibited high first discharge capacities of 1272, 1280, and 1308 mAh g^{-1} for

Research Article
doi.org/10.1002/batt.202500497
Chemistry Europe
European Chemical Societies Publishing

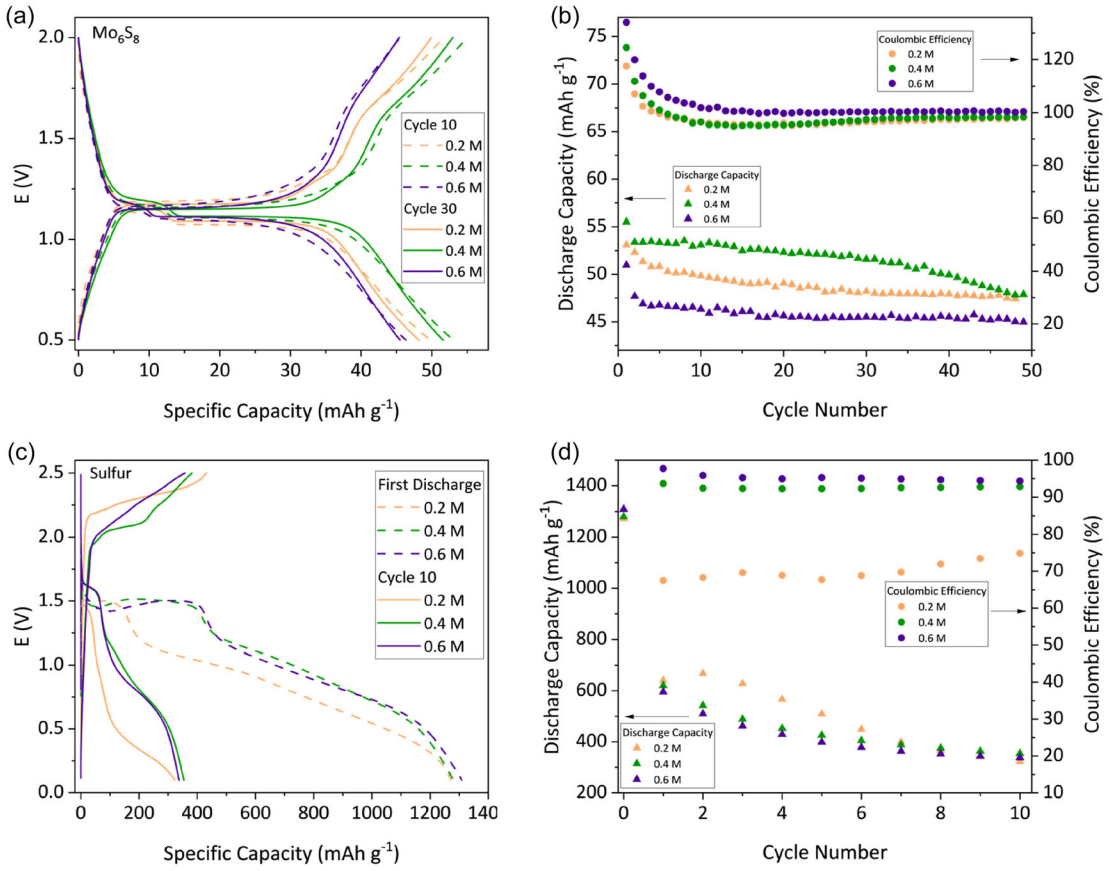

Figure 4. Electrochemical testing of Chevrel phase at C/10 in the voltage window from 0.5 to 2.0 V. a) Discharge/charge voltage profiles in the 10th and 30th cycle; b) discharge capacity and Coulombic efficiency for different MgAlhfip/G2 concentrations. Electrochemical testing of the sulfur cathode at C/10 in the voltage window from 0.1 to 2.5 V. c) Discharge/charge voltage profiles in first discharge and 10th cycle; d) discharge capacity and Coulombic efficiency for different MgAlhfip/G2 concentrations.

0.2, 0.4, and 0.6 M, respectively (Figure 4c), followed by a rapid capacity drop, typical for Mg-S systems.[32] The capacity drop was faster for 0.4 and 0.6 M concentrations, while 0.2 M exhibited a more gradual one. The galvanostatic discharge/charge curves displayed two voltage plateaus: a short one around 1.5 V, corresponding to the initial sulfur conversion and long-chain polysulfide reactions, and the second, more sloped plateau below 1.2 V, associated with the reduction of shorter polysulfides.[30] Interestingly, these plateaus are retained in more concentrated electrolytes in the later cycles, while they become less pronounced in 0.2 M electrolyte (Figure 4c). Similarly, the 0.6 M electrolyte displayed the highest Coulombic efficiencies, with an efficiency of 94% in the 10th cycle (Figure 4d). Testing of sulfur electrodes confirms that higher electrolyte concentrations increase the Coulombic efficiency, as already observed in the case of the Chevrel phase cathode. Moreover, higher salt concentration and increased viscosity of MgAlhfip electrolytes can reduce the polysulfide shuttle effect,[33] which is especially evident at 0.4 and 0.6 M electrolyte concentrations.

Among redox-active organic materials, the poly(anthraquinone sulfide) (PAQS) polymer was selected due to the excellent reversibility of the AQ active group in WCA-based Mg electrolytes.[34,35] PAQS has a theoretical capacity of 225 mAh g^{-1} with a discharge potential of around 1.6 V, making it well-suited for the stability windows of different Mg electrolytes. Electrochemical testing revealed that PAQS initially exhibited very high-capacity utilization, followed by a sharp initial decrease, which became more gradual in the later cycles. All three electrolyte concentrations exemplified rapid capacity loss, falling below 80 mAh g^{-1} of capacity in the 10th cycle (**Figure 5**a). The less concentrated electrolytes—0.2 and 0.4 M, despite higher initial capacities (around 160 mAh g^{-1}, Figure S10, Supporting Information), exhibited higher capacity fade, while the 0.6 M electrolyte, with the lowest starting value (117 mAh g^{-1}), demonstrated relatively better stability in later cycles. These results indicate that the PAQS active material suffers from a pronounced capacity fading regardless of the electrolyte concentration, likely due to active material dissolution. Higher salt concentrations reduced initial capacity utilization and slowed down the capacity fading, most likely due to lower polymer solubility in more concentrated electrolytes. However, upon continued cycling, the discharge capacities became relatively similar and stabilized around 60 mAh g^{-1} for all three concentrations. More pronounced differences between PAQS cells are observed in the Coulombic efficiencies (Figure 5b). The 0.2 M exhibited the lowest efficiency (around 58% in the 15th cycle, rising to 70% in later cycles),

Research Article
doi.org/10.1002/batt.202500497
Chemistry Europe
European Chemical Societies Publishing

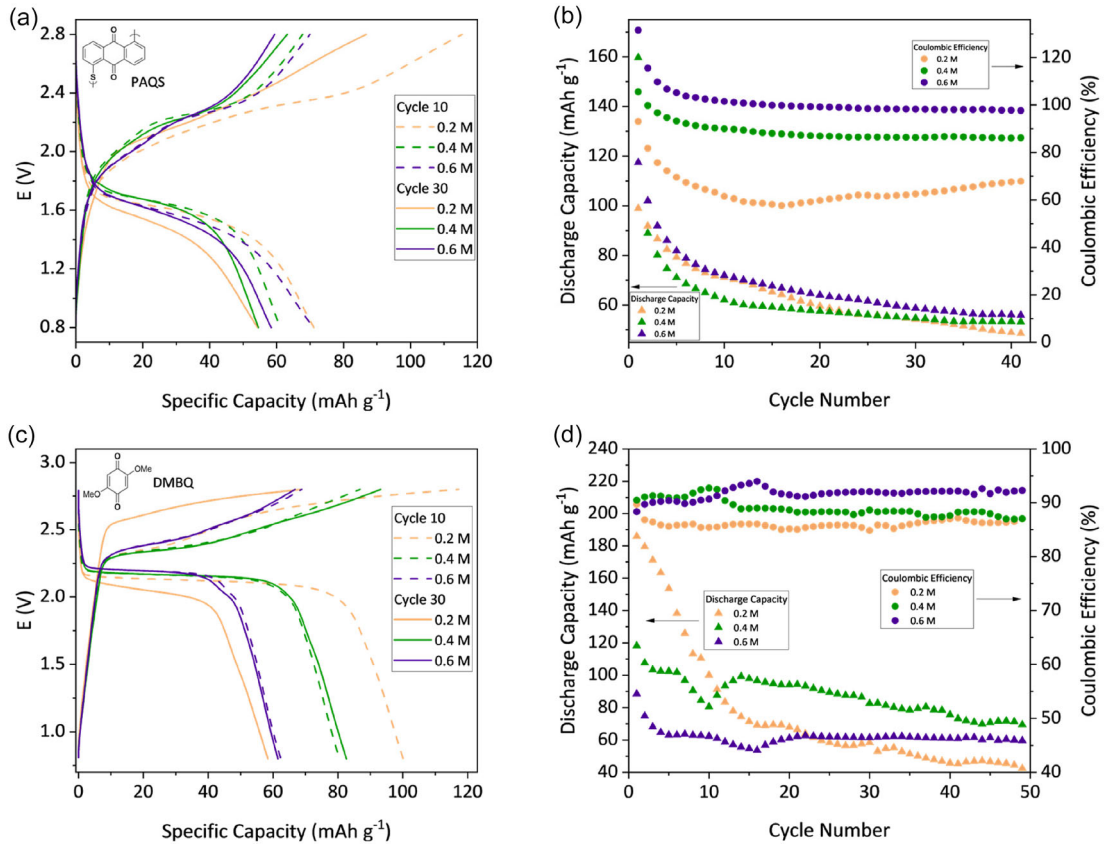

Figure 5. Electrochemical testing of PAQS active material at C/2 in the voltage window from 0.8 to 2.8 V. a) Discharge/charge voltage profiles in the 10th and 30th cycle; b) discharge capacity and Coulombic efficiency for different MgAlhfip/G2 concentrations. Electrochemical testing of DMBQ electrode at C/5 in the voltage window from 0.8 to 2.8 V. c) Discharge/charge voltage profiles in the 10th and 30th cycle; d) discharge capacity and Coulombic efficiency for different MgAlhfip/G2 concentrations.

0.4 M had an initial efficiency close to 100% which later dropped below 90%, and for 0.6 M electrolyte the efficiency initially exceeded 100%—a phenomenon commonly observed for organic electrodes with Mg electrolytes due to electrode swelling and gradually increasing capacity utilization in the starting cycles,[36,37] before stabilizing around 98%.

Furthermore, we investigated a simple monomer organic material based on the benzoquinone electroactive group, 2,5-dimethoxy-1,4-benzoquinone (DMBQ), due to its high theoretical capacity (319 mAh g^{-1}) and higher redox potential compared to PAQS. During initial discharge, all cells exhibited a relatively high discharge voltage plateau at 2.2 V and relatively high discharge capacities between 254 and 279 mAh g^{-1} (Figure S10c, Supporting Information), demonstrating high capacity utilization. However, again, a fast capacity decline is observed for all three concentrations (Figure 5c). Regarding Coulombic efficiency, all three concentrations exhibited relatively stable efficiencies throughout cycling, with values of 86%, 89%, and 92% observed for 0.2, 0.4, and 0.6 M, respectively (Figure 5d). These values are considerably lower than in the case of PAQS, and might be attributed to a combination of electrolyte degradation, likely happening at the higher redox potential, and possible DMBQ active material shuttling.

Recently, polyaniline (PANI) has been successfully applied to Mg-organic batteries.[23] It is especially interesting due to its ability to act as both p-type and n-type material (enabling storage of both cations and anions) and high redox potential.[38] We tested the emeraldine base form of PANI in the voltage window up to 3.1 V, which is beyond the typical voltage limit of glyme-based Mg electrolytes. As shown in Figure S11, Supporting Information, the specific capacities measured during the first cycle exceeded the first discharge capacities, indicating that some electrochemical conversion reaction is happening in the first cycle. Furthermore, two voltage plateaus were observed during cycling—one above 2.0 V and the second below 1.5 V. They were especially prominent in the initial cycles, but with further cycling, they became less distinguishable, and PANI capacities stabilized around 140 mAh g^{-1} (for 0.6 M), but a certain difference in the potential and capacity contribution of the higher voltage plateau remained among different electrolytes. Compared to PAQS, PANI exhibited a slower capacity fade, with improved electrochemical stability over a wide voltage range (0.5–3.1 V). However, observed stability at high potential can also be connected with the fact that the material undergoes a p-type electrochemical mechanism instead of n-type, as PAQS and DMBQ, or a much better oxidative stability of PANI material. P-type electrochemical mechanism could also explain

better PANI capacity utilization in the electrolytes with higher concentrations of salt.

3. Conclusion

In this study, we focused on state-of-the-art WCA-based electrolyte, MgAlhfip/G2, and conducted a systematic investigation into how different concentrations affect its physicochemical properties, salt–solvent interactions, and, most importantly, electrochemical performance. Regarding electrolyte conductivity, a typical parabolic trend as salt concentration increased was observed, with maximum conductivity at 0.4 M concentration. Raman measurements revealed a reduced presence of free glyme solvent in more concentrated electrolytes. However, no significant differences were observed during LSV tests. The electrochemical evaluation showed that Mg electrolyte concentration affects the performance of the Mg metal anode and all tested cathodes. While all three concentrations displayed good Mg plating/stripping activity, the 0.6 M electrolyte exhibited the most stable cycling and the highest Coulombic efficiency with prolonged cycling. When Mg plating/stripping included OCV rest periods, plating/stripping efficiency dropped for all concentrations, indicating a clear need for further improvement of Mg electrolytes and a requirement to design a stable metal/electrolyte interphase. Overall, lower concentrations resulted in more erratic plating/stripping efficiencies, whereas the 0.6 M concentration had the most stable electrochemical behavior, indicating the beneficial effect of a higher salt amount and derived Mg metal/electrolyte interphase.

When paired with different active cathode materials, the influence of electrolyte concentration on overpotentials and capacity utilization varied among the materials used. Nevertheless, the highest electrolyte concentration typically led to the highest Coulombic efficiencies. Electrochemical cycling of a Chevrel phase cathode showed relatively stable performance and minor differences between electrolyte concentrations. On the other hand, sulfur cathodes demonstrated relatively good initial capacity utilization, followed by rapid capacity fade and limited reversibility for all electrolytes. Organic cathodes (PAQS, DMBQ, PANI) exhibited better reversibility coupled with gradual capacity fade, indicating that organic material dissolution seems to be more pronounced in Mg electrolytes than in Li electrolytes,[39] irrespective of the use of monomer or polymer compounds. This highlights the need not only to transfer organic materials with proven electrochemical performance in Li electrolytes for use with Mg but also to carefully select and design more stable organic materials.

Overall, our results emphasize that more concentrated MgAlhfip electrolytes with a lower amount of glyme solvent generally improve cathode cycling efficiency by reducing parasitic side reactions at higher voltage limits, while ensuring a more stable Mg plating/stripping behavior. Although this comes at a cost of increased electrolyte viscosity and potential electrode wettability issues, it argues for the use of more concentrated Mg electrolytes in future studies. Nevertheless, issues related to the theoretical capacity utilization of the active material and long-term capacity retention remain unresolved and require further improvements either through the design of the active material or the optimization of the electrolyte. From a practical point of view, higher salt concentrations could lead to more expensive Mg electrolytes. To further optimize the electrolytes, it is therefore important to consider the specific electrodes used in Mg cells and to design the electrolyte properties to meet the requirements of the respective active material at a reasonable cost.

4. Experimental Section

Salt Synthesis and Characterization. Electrolyte Preparation

MgAlhfip salt was synthesized according to the published procedure[12] with a modification in the isolation step. Detailed procedure is described in the Supporting Information. The electrolytes were prepared by adding the appropriate amount of salt into measuring flasks and diluting them to the mark to obtain the chosen concentrations. A detailed procedure and approximate salt-to-solvent molar ratios can be found in the SI (Table S1, Supporting Information), as well as the physicochemical characterization of the prepared electrolytes measured at 25 °C.

Material Preparation

Mo_6S_8 was synthesized by annealing elemental copper, molybdenum, and sulfur mixtures (5 g) with excess sulfur at a stoichiometry of $Cu_2Mo_6S_{8.5}$. The mixture was loaded into Swagelok stainless steel vessels under an argon atmosphere. These vessels were then placed in a preheated furnace at 1000 °C for 20 min. The ratio between the reactant and total reactor volumes was 1:2. The resulting products were ground using a mortar and pestle into a fine powder with sub-micrometer-sized particles. They were characterized by XRD as copper Chevrel phases. Copper was extracted through a mild oxidation process using an I_2/acetonitrile solution, yielding Mo_6S_8 cathode material.

The carbon-sulfur composite was prepared by impregnation of ENSACO 350 G carbon (Imerys Graphite & Carbon) with sulfur to give a sulfur carbon composite with 33 wt % sulfur. Briefly, carbon and sulfur were ball-milled for 30 min on a Retsch PM100 at 300 rpm in a mass ratio of 67:33. The resulting mixture was then heated in a quartz tube furnace under an inert argon atmosphere, with a heating ramp of 0.2 °C min^{-1} to 155 °C, where it was held for 5 h. Afterward, the composite was cooled to room temperature at a rate of 0.5 °C min^{-1}.

Poly(anthraquinone sulfide) (PAQS) was synthesized through a polycondensation reaction between 1,5-dichloroantraquinone and Na_2S in NMP with in situ added MWCNT (10 wt %, NTL C-grade).[40] Detailed procedure can be found in the Supporting Information.

PANI (polyaniline, emeraldine base, average Mw ≈ 50 000) was purchased from Fluka and used as an active material for cathode preparation.

2,5-Dihydroxybenzoquinone was suspended in methanol, then concentrated HCl was added. The reaction mixture was stirred overnight at room temperature, and a change of color from orange to yellow was observed. Subsequently, the reaction mixture was filtered and washed with cool methanol. The dried product gave the final product 2,5-dimethoxybenzoquinone (DMBQ) with a 91% yield.[41]

Electrode Preparation

Cathodes were prepared by mixing the active material (Mo_6S_8, PAQS, PANI, DMBQ) with Printex XE2 (Degussa) carbon black and a PTFE (Sigma–Aldrich, 60%) binder in a 60:30:10 weight ratio. Sulfur cathodes were prepared using a carbon-sulfur composite, Super C65, and PTFE binder in the same weight ratio. Printex cathodes were prepared by mixing Printex XE2 and PTFE in a mass ratio of 75:25. All components, along with isopropanol were added into a ball mill jar and homogenized for 30 min using a Retsch PM100 at 300 rpm. The resulting composite matrices were then rolled between a glass plate and a sheet of baking paper to form self-standing electrodes. All composites were cut into 12 mm self-standing electrodes, dried overnight at 50 °C, and transferred into the Ar-filled glovebox. Loading of active materials ranged between 1.5 and 3.7 mg cm^{-2} for Mo_6S_8, around 0.8 mg cm^{-2} for sulfur, between 0.8 and 1.7 mg cm^{-2} for PAQS, 1.1 and 1.4 mg cm^{-2} for PANI, 1.5 and 2.1 mg cm^{-2} for DMBQ, and between 0.6 and 2.6 mg cm^{-2} for Printex cathodes.

Electrochemical Characterization

Electrochemical tests were performed in galvanostatic mode using a VMP3 potentiostat from Bio-Logic S.A. with two-electrode Swagelok-type cells. For all tests, magnesium foil (0.1 mm, 99.95%, Changsha Rich Nonferrous Metals) was polished with P1200 sandpaper inside a glovebox before use as the anode. For LSV tests, a platinum disc (Pt, Goodfellow, 99.9%) and carbon-coated aluminum foil (CC Al, MSE Supplies, 99.9%) as working electrodes, together with Mg metal foil as the counter electrode, were used.

Three experimental Mg plating/stripping protocols were used. In the first one, Mg plating was performed at a current density of 1 mA cm^{-2} for 1 h, followed by stripping until the cutoff voltage of 2 V, with a platinum disc as the working electrode and Mg metal foil as the counter electrode. The second protocol included macro reversibility measurements, where a five times larger amount of Mg metal was initially plated on the working electrode, but only one-fifth of it was cycled. After 45 cycles of partial plating and stripping, the remaining Mg deposits were fully stripped until reaching 2 V. The third protocol resembled the first one but included different OCV periods after Mg plating on the Pt working electrode. Initially, 10 cycles of Mg plating/stripping without OCV pause periods were performed (regular cycling). Subsequently, OCV periods of 1, 2, and 5 h were introduced after each plating half-cycle.

Cells used in the first and second protocols were assembled with three layers of a glass fiber separator (GF/A, Whatman, 260 µm) and wetted with ≈100 µl of electrolyte. For the third protocol, cells were assembled with five layers of the glass fiber separator and wetted with ≈200 µl of electrolyte.

Electrochemical testing of Mg cells with cathodes was conducted at different C rates. Mo_6S_8 cathodes were tested at C/10 (12.9 mA g^{-1}), PAQS and PANI polymer cathodes were tested at C/2 (112.5 and 125 mA g^{-1}, respectively), DMBQ was tested at C/5 (63.8 mA g^{-1}), sulfur cathodes at C/10 (167.2 mA g^{-1}) and Printex cathodes with current density of 50 mA g^{-1}, which was reduced to 10 mA g^{-1} after 10 cycles. All cells were assembled with three layers of the glass fiber separator wetted with ≈100 µl of electrolyte.

Scanning Electron Microscopy (SEM)

Scanning electron microscopy (SEM) analysis was performed using an FE-SEM Supra 35 VP (Carl Zeiss) at an accelerating voltage of 1.5 and 2 kV with an InLens detector. For Mg deposit sample preparation, cells with carbon-coated Al foil as the working electrode and Mg metal as the counter electrode with different concentrations of electrolytes were assembled. One Celgard 2400 separator (CG) was added to three glass fiber separators and placed on the working electrode to prevent the entanglement of separator fibers with Mg metal deposits. After plating at a current density of 1 mA cm^{-2} for 3 min, the cells were disassembled in the glovebox. The working electrode with Mg deposits was carefully removed from the cell and washed with G1. Samples were transferred to the SEM chamber under vacuum using a specifically designed sample holder to prevent their decomposition in the ambient atmosphere.

IR and Raman Spectroscopy

IR characterization was conducted inside the glovebox using an ATR-IR Alpha II (Bruker) spectrometer equipped with a diamond crystal. Spectra were recorded at room temperature, averaging 48 scans over a range of 4000–400 cm^{-1} with a resolution of 4 cm^{-1}.

Raman spectra of the solvents and electrolytes were obtained using a Bruker Ram II Raman spectrometer equipped with a 1064 nm excitation laser. Each spectrum was averaged over 512 scans at a resolution of 4 cm^{-1}, covering the spectral range from 50 to 3600 cm^{-1}. The samples were sealed in airtight quartz tubes (1 cm thickness) under an argon atmosphere for measurement.

Acknowledgements

The authors gratefully acknowledge Prof. Doron Aurbach from Bar Ilan University, Israel, for providing Chevrel phase (Mo_6S_8) active material and Nemanja Latas from the National Institute of Chemistry, Slovenia, for providing the sulfur cathode materials used in this work. A.M., T.P., O.L., R.D., and J.B. would like to acknowledge the financial support of the Slovenian Research and Innovation Agency (ARIS) under research programs P2−0423 and N2−0279. PhD position of A.M. is funded by ARIS through the Scientists4Future Slovenia project (MSCA-COFUND-SE/2023). A.P. and T.P. gratefully acknowledge funding from the European Research Council (ERC) under the European Union's Horizon 2020 research and innovation programme (grant agreement No. 101089281) and the Spanish Agencia Estatal de Investigación Severo Ochoa Programme for Centres of Excellence in R&D (CEX2023- 01263). K.P. acknowledges financial support from public call MS-ERC-FS/2017-002, Ministry of Education, Science and Sport (MIZS) for funding the M.Era-net project InsBioration (call 2021).

Conflict of Interest

The authors declare no conflict of interest.

Data Availability Statement

The data that support the findings of this study are available from the corresponding author upon reasonable request.

Keywords: cathode compatibility · different metal plating/stripping procedures · electrolyte speciation · Mg electrolyte · physicochemical properties

[1] C. Wei, L. Tan, Y. Zhang, Z. Wang, J. Feng, Y. Qian, *Energy Storage Mater.* **2022**, *52*, 299.
[2] R. Dominko, J. Bitenc, R. Berthelot, M. Gauthier, G. Pagot, V. Di Noto, *J. Power Sources* **2020**, *478*, 229027.
[3] R. Mohtadi, O. Tutusaus, T. S. Arthur, Z. Zhao-Karger, M. Fichtner, *Joule* **2021**, *5*, 581.
[4] Q. Sun, S. Luo, R. Huang, Q. Liu, X. Yan, Y. Lin, S. Yan, X. Lin, *Energy Storage Mater.* **2025**, *80*, 104351.
[5] O. Tutusaus, R. Mohtadi, T. S. Arthur, F. Mizuno, E. G. Nelson, Y. V. Sevryugina, *Angew. Chem.* **2015**, *127*, 8011.
[6] Z. Zhao-Karger, M. E. G. Bardaji, O. Fuhr, M. Fichtner, *J. Mater. Chem. A.* **2017**, *5*, 10815.
[7] S. Li, J. Zhang, S. Zhang, Q. Liu, H. Cheng, L. Fan, W. Zhang, X. Wang, Q. Wu, Y. Lu, *Nat. Energy* **2024**, *9*, 285.
[8] T. Pavčnik, M. Radi, O. Lužanin, R. Dedryvère, D. S. Tchitchekova, A. Ponrouch, J. Bitenc, R. Dominko, *J. Power Sources* **2025**, *626*, 235711.
[9] J. Luo, Y. Bi, L. Zhang, X. Zhang, T. L. Liu, *Angew. Chem.* **2019**, *131*, 7041.
[10] W. Ren, D. Wu, Y. NuLi, D. Zhang, Y. Yang, Y. Wang, J. Yang, J. Wang, *ACS Energy Lett.* **2021**, *6*, 3212.
[11] J. T. Herb, C. A. Nist-Lund, C. B. Arnold, *ACS Energy Lett.* **2016**, *1*, 1227.
[12] T. Mandai, Y. Youn, Y. Tateyama, *Mater. Adv.* **2021**, *2*, 6283.
[13] T. Pavčnik, M. Lozinšek, K. Pirnat, A. Vizintin, T. Mandai, D. Aurbach, R. Dominko, J. Bitenc, *ACS Appl. Mater. Interfaces* **2022**, *14*, 26766.
[14] T. Pavčnik, J. Imperl, M. Kolar, R. Dominko, J. Bitenc, *J. Mater. Chem. A.* **2024**, *12*, 3386.
[15] T. Pavčnik, in PhD Thesis. University of Ljubljana (SLO **2023**).
[16] E. N. Keyzer, J. Lee, Z. Liu, A. D. Bond, D. S. Wright, C. P. Grey, *J. Mater. Chem. A.* **2019**, *7*, 2677.
[17] T. Mandai, *ACS Appl. Mater. Interfaces* **2020**, *12*, 39135.
[18] K. Fujii, M. Sogawa, N. Yoshimoto, M. Morita, *J. Phys. Chem. B.* **2018**, *122*, 8712.
[19] I. Raabe, K. Wagner, K. Guttsche, M. Wang, M. Grätzel, G. Santiso-Quiñones, I. Krossing, *Chem. Eur. J.* **2009**, *15*, 1966.
[20] N. J. Leon, S. Ilic, X. Xie, H. Jeong, Z. Yang, B. Wang, E. W. C. Spotte-Smith, C. Stern, N. Hahn, K. Zavadil, L. Cheng, K. A. Persson, J. G. Connell, C. Liao, *J. Phys. Chem. Lett.* **2024**, *15*, 5096.
[21] M. Salama, I. Shterenberg, H. Gizbar, N. N. Eliaz, M. Kosa, K. Keinan-Adamsky, M. Afri, L. J. W. Shimon, H. E. Gottlieb, D. T. Major, Y. Gofer, D. Aurbach, *J. Phys. Chem. C.* **2016**, *120*, 19586.
[22] D. M. Driscoll, N. K. Dandu, N. T. Hahn, T. J. Seguin, K. A. Persson, K. R. Zavadil, L. A. Curtiss, M. Balasubramanian, *J. Electrochem. Soc.* **2020**, *167*, 160512.
[23] C. Li, R. D. Guha, A. Shyamsunder, K. A. Persson, L. F. Nazar, *Energy Environ. Sci.* **2024**, *17*, 190.
[24] I. Krossing, *Chem. Eur. J.* **2001**, *7*, 490.
[25] R. Zhu, T. Yabu, C. Yang, H. Yang, A. Nasu, T. Mandai, M. Matsui, H. Kobayashi, *Adv. Energy Mater.* **2025**, *15*, 2502050.
[26] B. D. Adams, J. Zheng, X. Ren, W. Xu, J.-G. Zhang, *Adv. Energy Mater.* **2018**, *8*, 1702097.
[27] I. Shterenberg, M. Salama, H. D. Yoo, Y. Gofer, J.-B. Park, Y.-K. Sun, D. Aurbach, *J. Electrochem. Soc.* **2015**, *162*, A7118.
[28] A. K.č Lautar, J. Bitenc, T. Rejec, R. Dominko, J.-S. Filhol, M.-L. Doublet, *J. Am. Chem. Soc.* **2020**, *142*, 5146.
[29] D. Aurbach, Z. Lu, A. Schechter, Y. Gofer, H. Gizbar, R. Turgeman, Y. Cohen, M. Moshkovich, E. Levi, *Nature* **2000**, *407*, 724.
[30] A. Robba, A. Vizintin, J. Bitenc, G. Mali, I. Arčon, M. Kavčič, M. Žitnik, K. Bučar, G. Aquilanti, C. Martineau-Corcos, A. Randon-Vitanova, R. Dominko, *Chem. Mater.* **2017**, *29*, 9555.
[31] Z. Li, A. Welle, S. Vincent, L. Wang, S. Fuchs, S. Riedel, A. Roy, D. Bosubabu, J. M. García-Lastra, M. Fichtner, Z. Zhao-Karger, *Adv. Energy Mater.* **2023**, *13*, 2302905.
[32] S. D.č Talian, A. Vizintin, J. Bitenc, G. Aquilanti, A. Randon-Vitanova, M. Gaberšček, R. Dominko, *ChemElectroChem* **2021**, *8*, 1062.
[33] T. Gao, S. Hou, F. Wang, Z. Ma, X. Li, K. Xu, C. Wang, *Angew. Chem.* **2017**, *129*, 13711.
[34] T. Pavčnik, J. Bitenc, K. Pirnat, R. Dominko, *Batteries Supercaps* **2021**, *4*, 815.
[35] Y. Xiu, Z. Li, V. B. Parambath, Z. Ding, L. Wang, A. Reupert, M. Fichtner, Z. Zhao-Karger, *Batteries Supercaps* **2021**, *4*, 1850.
[36] A. Vizintin, J. Bitenc, A. K.č Lautar, J. Grdadolnik, A. R. Vitanova, K. Pirnat, *ChemSusChem* **2020**, *13*, 2328.
[37] J. Bitenc, K. Pirnat, E. Žagar, A. Randon-Vitanova, R. Dominko, *J. Power Sources* **2019**, *430*, 90.
[38] P. Jiménez, E. Levillain, O. Alévêque, D. Guyomard, B. Lestriez, J. Gaubicher, *Angew. Chem.* **2017**, *129*, 1575.
[39] M. Yao, H. Senoh, S. Yamazaki, Z. Siroma, T. Sakai, K. Yasuda, *J. Power Sources* **2010**, *195*, 8336.
[40] Z. Song, H. Zhan, Y. Zhou, *Chem. Commun.* **2009**, *4*, 448.
[41] J. Bitenc, N. Lindahl, A. Vizintin, M. E. Abdelhamid, R. Dominko, P. Johansson, *Energy Storage Mater.* **2020**, *24*, 379.

Manuscript received: June 30, 2025
Revised manuscript received: August 12, 2025
Version of record online: